REPORT DOCUMENTATION PAGE

The public reporting burden for this collection of information is estimated to average 1 hour per response, including the time for reviewing instructions, searching existing data sources, gathering and maintaining the data needed, and completing and reviewing the collection of information. Send comments regarding this burden estimate or any other aspect of this collection of information, including suggestions for reducing the burden, to the Department of Defense, Executive Service Directorate (0704-0188). Respondents should be aware that notwithstanding any other provision of law, no person shall be subject to any penalty for failing to comply with a collection of information if it does not display a currently valid OMB control number.

PLEASE DO NOT RETURN YOUR FORM TO THE ABOVE ORGANIZATION.

1. REPORT DATE (DD-MM-YYYY)	2. REPORT TYPE	3. DATES COVERED (From - To)
27-07-2010	Final Report	APR 07-MAR 10

4. TITLE AND SUBTITLE
MULTI-RESOLUTION IMAGING OF ELECTRON DYNAMICS IN NANOSTRUCTURE INTERFACES

5a. CONTRACT NUMBER
FA9550-07-1-0338

5b. GRANT NUMBER
FA9550-07-1-0338

5c. PROGRAM ELEMENT NUMBER

6. AUTHOR(S)
Dr Jiwoong Park

5d. PROJECT NUMBER

5e. TASK NUMBER

5f. WORK UNIT NUMBER

7. PERFORMING ORGANIZATION NAME(S) AND ADDRESS(ES)
Cornell University
373 Pine Tree Road
Ithaca, NY 14850

8. PERFORMING ORGANIZATION REPORT NUMBER

9. SPONSORING/MONITORING AGENCY NAME(S) AND ADDRESS(ES)
Air Force Office of Scientific Research
875 North Randolf Street Suite 325, Room 3112
Arlington, VA 22203-1768

10. SPONSOR/MONITOR'S ACRONYM(S)
AFOSR

11. SPONSOR/MONITOR'S REPORT NUMBER(S)

12. DISTRIBUTION/AVAILABILITY STATEMENT
The information in this report is unclassified and can be made available to public.

13. SUPPLEMENTARY NOTES

14. ABSTRACT
This final report describes the development and the application of two novel optoelectronic microscope techniques ("photocurrent imaging" and "photothermal current imaging") for electronic devices fabricated based on carbon nanotubes and thin film organic materials, as funded by the AFOSR grant. We showed that individual carbon nanotubes can be imaged and characterized using the photothermal current microscopy for the first time. In particular, this technique allows the imaging and electrical characterization of carbon nanotubes one by one even when only one pair of metal electrodes are used to contact all of them. This eliminates the need for individual electrodes for each carbon nanotube, which is time consuming and expensive. With this, the gate dependent electrical conductivity can be measured as well, thus enabling differentiation of metallic carbon nanotubes from semiconducting ones. In pentacene transistors, we used scanning photocurrent microscopy to study spatially resolved photoelectric response of pentacene thin films, which showed that point contacts formed near the hole injection points limit the overall performance of the device. In addition, we estimate the contact resistance of individual contact for the first , which is of the order of ~1 GOhms.

15. SUBJECT TERMS
photothermal current microscopy, carbon nanotube transistor, pentacene transistor, contact resistance, hole injection

16. SECURITY CLASSIFICATION OF:			17. LIMITATION OF ABSTRACT	18. NUMBER OF PAGES	19a. NAME OF RESPONSIBLE PERSON
a. REPORT	b. ABSTRACT	c. THIS PAGE			Dr. Harold Weinstock
U	U	U	UU		19b. TELEPHONE NUMBER (Include area code) 703-696-5944

Reset

FA9550-07-1-0338
Final Report

COVER SHEET

Title:
MULTI-RESOLUTION IMAGING OF ELECTRON DYNAMICS IN NANOSTRUCTURE INTERFACES

Date:
July 27, 2010

Reporting Period:
Apr 07- Mar 10

Technical area
   Physics and Electronics

Organizations
   Cornell University, Ithaca, NY

Program Manager
   Dr. Harold Weinstock

TECHNICAL POC	ADMINISTRATIVE POC
Last name: **Park**	Last name: **Prince**
Salutation: **Prof.** First name: **Jiwoong**	Salutation: **Ms** First name: **Amie**
Street Address :	Street Address:
B50A Baker Laboratory	**373 Pine Tree Road**
Dept. Of Chemistry and Chemical Biology	**Office of Sponsored Programs**
Cornell University	**Cornell University**
Ithaca, NY 14853	**Ithaca, NY 14850**
Telephone: (607) 254-3339	**Telephone: (607)-255-5337**
Fax: (607) 255-4137	**Fax: (607) 255-5058**
Email: jp275@cornell.edu	**Email: ajp246@cornell.edu**

Executive Summary

This final report describes the development and the application of two novel optoelectronic microscope techniques ("photocurrent imaging" and "photothermal current imaging") for studying electron dynamics near the interfaces of electronic devices fabricated based on carbon nanotubes and thin film organic materials, as funded by the AFOSR grant (FA9550-07-1-0338). In carbon nanotube devices, we showed that individual carbon nanotubes can be imaged and characterized using the photothermal current microscopy for the first time. In particular, this technique allows the imaging and electrical characterization of carbon nanotubes one by one even when only one pair of metal electrodes are used to contact all of them. This eliminates the need for individual electrodes for each carbon nanotube, which is time consuming and expensive. With this, the gate dependent electrical conductivity can be measured as well, thus enabling differentiation of metallic carbon nanotubes from semiconducting ones. In pentacene transistors, we used scanning photocurrent microscopy to study spatially resolved photoelectric response of pentacene thin films, which showed that point contacts formed near the hole injection points limit the overall performance of the device. In addition, we estimate the contact resistance of individual contact for the first time, which is of the order of ~1 GΩ per contact point.

TECHNICAL DESCRIPTION OF WORK

A. Introduction

Over the past decades, electronic and optoelectronic devices incorporating low-dimensional materials have emerged as promising candidates for supplementing, and in some cases even supplanting, conventional devices. However, precise control over the electronic properties of such systems remains a fundamental challenge to this day. This is in large part due to the myriad of processes occurring at different length scales within the device.

For example, the operation of a nanowire-based field effect transistor is affected by the electron and hole transport properties across the metal/nanostructure junction, buried interfaces between dissimilar materials as well as the main body of the nanostructure. Therefore, the efficiency and fidelity of device performance depend not only on the material itself but also critically on the junctions between them.

In order to fully understand the physics of device operation as well as to optimize device performance, one requires a powerful experimental tool with high spatial resolution to segregate and independently interrogate these distinct effects. Here, we describe our work involving a custom-built photoelectrical microscope in an effort to achieve these goals. In this setup, we raster a diffraction-limited, focused laser spot (usually λ = 658 nm, FWHM ~ 1 μm, power ~ 1 mW) across the surface of our device that is electrically addressed. We monitor the device current as a function of spot position simultaneously with reflected light intensity in order to determine the absolute position of the beam. Therefore, if the material is electrically responsive to the laser, we obtain a spatial map of the optoelectronic behavior of the device.

Under this AFOSR grant, we developed two novel photoelectric imaging techniques. Using these techniques, we studied two different materials of technological importance: carbon nanotubes and pentacene thin-films. We will explain these below in further detail.

Carbon nanotube devices were previously studied by various methods including optoelectronic measurements. Prior to this work, we have studied the photocurrent generated from band-bending at the contact and internal p-n junctions of carbon nanotube devices, yielding information on their spatial band structure. However, nanotubes are unique in that, beyond their interfacial properties, the material itself could possess varying electronic behaviors depending on its chirality. We have been able to exploit the photothermal effect to image the conductance of individual carbon nanotubes directly using our photoelectric technique, and then we extend the scheme to characterize large-scale nanotube transistors in parallel.

While pentacene thin-film transistors have existed for decades, various processing and fabrication parameters have been shown to impact their performance. In particular, for the technologically relevant bottom-contact, bottom gate geometry, energy barriers at the contact has been shown to limit hole injection. We find that pentacene films make point-like electrical contacts to the underlying gold electrodes and are able to image them with diffraction-limited resolution. We can further estimate the interfacial resistance associated with hole-injection at an individual point contact, and show that optical activation of one alone increases device current significantly.

B. Conductance Imaging of Carbon Nanotubes via the Photothermal Effect

The one-dimensional structure of carbon nanotubes[1] leads to a variety of remarkable optical[2] and electrical[3] properties that could be used to develop novel devices[4]. In the past, we and other

groups have used scanning photocurrent (SPC) microscopy to image the electronic band mapping of carbon nanotube transistors[6-9]. Although the photocurrent exhibits strong gate dependence, it is not a direct probe of device conductance because a photocurrent is also generated when the nanotube is turned "off." In contrast, the conductance of nanotubes is susceptible to changes in temperature[10,11]. Here, we induce local, optical heating of nanotube devices under applied bias using our photoelectric microscopy setup (Fig. 1a). We first developed an understanding of the relationship between the heat-induced current signal and the overall electrical conductance of the device for both metallic and semiconducting nanotubes, and then exploit this relation to image the gate-dependent conductance of various nanotube devices.
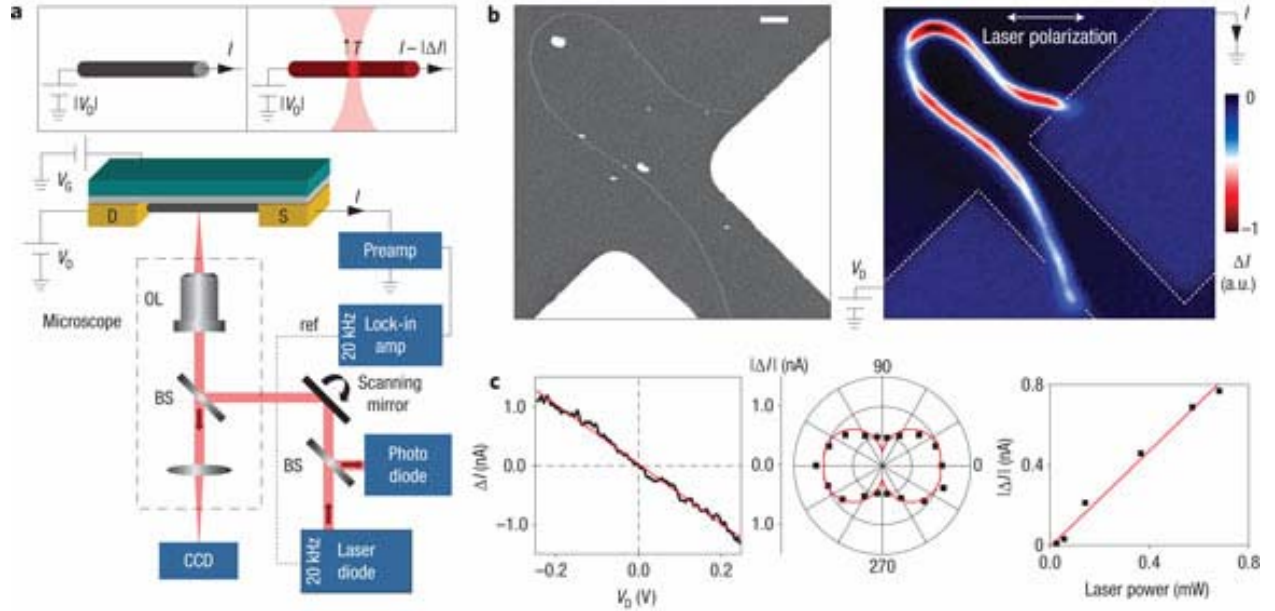
Fig. 1 a, Main panel: schematic of the scanning laser setup with simultaneous electrical measurement using a standard lock-in technique and the nanotube device studied. Top diagram showing mechanism of current change by laser heating. **b**, Left: AFM image of nanotube device D1. Scale bar, 1 μm. Right: current image of D1 corresponding to $V_D > 0$. The measurement circuit, electrodes and reflection image (overlaid) are shown for reference. **c**, Bias (left), polarization (middle) and laser power (right) dependence of current signal with the laser fixed on the nanotube.

On the left in Fig. 1b, we show an atomic force microscope (AFM) image of a representative device D1, a semi-metallic nanotube (diameter ~2.8 nm) contacted by two Pd/Cr/Au electrodes. On the right in Fig. 1b, we show in false-color a current image of D1 corresponding to $V_D > 0$. We can see a strong current signal along the entire length of the nanotube. The reflection image is overlaid, so that the electrodes (outlined with dashed lines) are visible, and the circuit used in the measurement is shown for reference. Comparison with the AFM image and the anisotropic laser polarization dependence of the current signal (Fig. 1c, middle) reveal that device current changes when the nanotube itself absorbs laser light. In particular, the polarity of ΔI suggests that laser induces a *conductance decrease* in our nanotube device. Furthermore, this signal anywhere along the nanotube is found to scale linearly with V_D (Fig. 1c, left), indicating that the conductance change $\Delta G = \dfrac{\Delta I}{V_D}$ is the fundamental quantity of interest in our experiment.

The mechanism through which light absorption can reduce the conductance of nanotubes is photothermal heating[5]. Under applied bias, DC current flows continuously through the device. However, as the beam is scanned over the nanotube, a fraction of light power is absorbed and converted into heat, increasing the temperature of the nanotube. This then changes device conductance by amount ΔG and creates a current differential, or *photo thermal current*, $\Delta I = \Delta G \cdot V_D$. Since we expect ΔG to be negative, ΔI is negative (positive) for positive (negative) V_D, as is the case in Fig. 1c. A schematic of this process is shown in the inset panels of Fig. 1a.
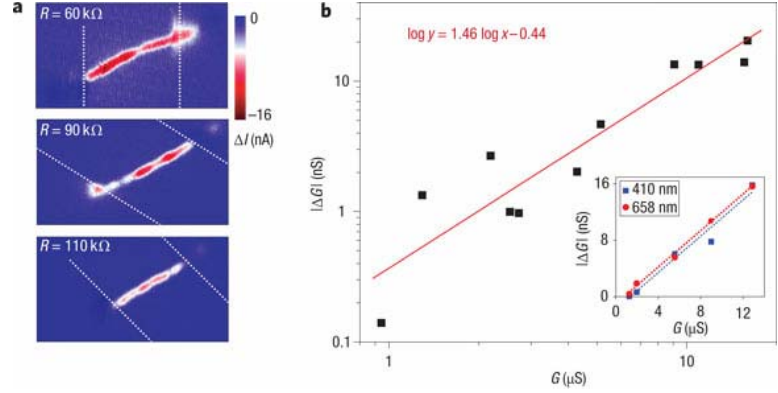

Fig. 2 a, Current images of carbon nanotube devices D2, D3 and D4 (resistances 60, 90 and 110 kΩ) with V_D = 0.2 V taken with standard lock-in. Electrode boundaries are marked with dotted lines. **b**, Main panel: magnitude of laser-induced conductance decrease $|\Delta G| = |\Delta I/V_D|$, averaged over the nanotube length, versus overall conductance G for 11 carbon nanotube devices in log–log scale. Inset: same plot for five devices using different laser wavelengths (410 nm, 658 nm, equal intensity) show similar heating behaviour for both wavelengths.

We can relate the heat-induced conductance decrease ΔG to $G(T)$ as $\Delta G = (dG/dT)\Delta T$, where T and ΔT are, respectively, the temperature and temperature increase of the nanotube, averaged along the nanotube length. Since we expect ΔT to scale linearly with irradiance for the light levels used in the experiment, we confirm this by measuring $|\Delta I|$ for **D1** as a function of laser power while fixing the laser on the nanotube, (Fig. 1c, right). The form of dG/dT can be deduced from the reported temperature dependence of the electrical conductivity of carbon nanotubes, which is inversely proportional to temperature T near room temperatures for both metallic[10] and semiconducting nanotubes in the "on" state[11]. Therefore, we expect that ΔG will scale monotonically with G with a power dependence close to unity.

Our measurements support this scaling. In Fig. 2a, we show current images of three devices **D2**, **D3**, **D4** with different resistances taken at identical bias and laser conditions. The photothermal current is overall largest (smallest) for the most (least) conductive device, a behaviour that is universally observed. In Fig. 2b (main panel), we plot $|\Delta G|$ (averaged along the nanotube length, standard lock-in) vs. G in log-log scale for eleven (semi-)metallic nanotubes of length ~5 μm under ~1 mW laser illumination. We see that $|\Delta G|$ increases monotonically with G for over an order of magnitude, with the line of best fit revealing a power dependence of 1.46 ± 0.19, substantiating our prediction if we assume similar ΔT for these devices.

We can study the gate dependence of electrical conductance of individual metallic and semiconducting nanotubes as well. In Fig. 3a, we show current images of semi-metallic nanotube **D1** at two different gate biases V_G = 0, 5 V, and V_D = 0.2 V. The overall current signal is clearly much stronger at V_G = 5V, suggesting that the nanotube becomes more conductive there. To study this behaviour more quantitatively, we scan the laser at a fixed location along the nanotube and measure photothermal current simultaneously with G while continuously varying V_G. In Fig. 3b, we plot $|\Delta G|$ (blue dots) and G (black solid line) as a function of V_G. We see that the two quantities track closely for all values of V_G. The odd dip in the transport curve at V_G < -3 V could
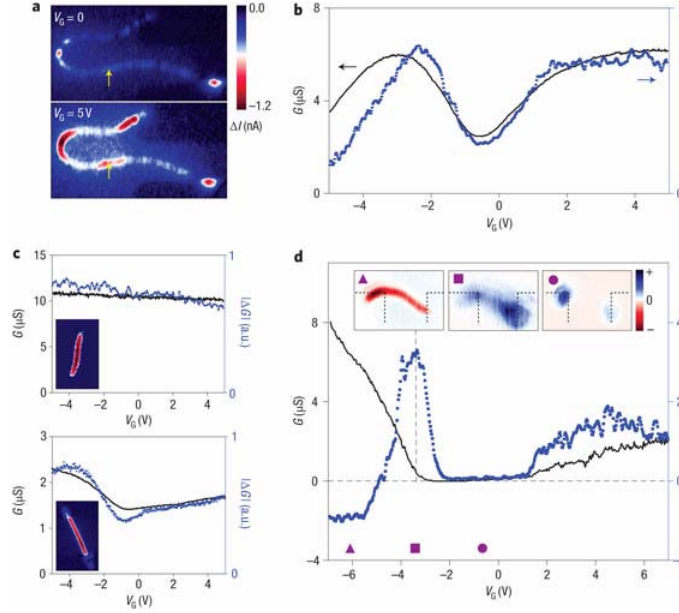
Fig. 3 a, Current images of semi-metallic device D1 with V_D = 0.2 V, V_G = 0 and 5 V taken with standard lock-in. **b**, $|\Delta G|$ (blue dots), measured with the laser fixed on the arrow shown in **a**, and G (black line, measured simultaneously) versus V_G. **c**, ΔG and G versus V_G for metallic and semi-metallic carbon nanotube devices D5 (top) and D6 (bottom). Insets: current images of each device. **d**, ΔG and G versus V_G for semiconducting device D7 shows conductance enhancement close to turn-off. Insets: Photothermal current images at different values of gate bias (indicated by corresponding markers), tuned to turn the device on (left) and off (right). Between these two states, conductance enhancement (middle) is observed.

be due to defects more prevalent at these nanotube lengths[20]. For all metallic and semi-metallic devices measured to date (~10), we observe a close correspondence between the gate dependences of ΔG and G. In Fig. 3c, we show similar plots for devices **D5** and **D6** that exhibit this correspondence at all gate biases, while their current images are shown in the insets.

We have also performed the same measurements on an individual semiconducting nanotube device **D7** with a well defined bandgap (Fig. 3d). We see that the laser induces photothermal current when the transistor is in the "on" state at negative V_G (left inset), while it apparently disappears altogether in the nanotube body once the device is "off" (right inset). Conductance is, however, *enhanced* upon laser illumination when V_G is tuned between the two regimes (middle inset). This conductance enhancement, which is strongest near the conductance turn-off (see the blue curve in the main panel), is likely due to a laser-induced thermal excitation of additional carriers[13].

C. Large-scale, Parallel Imaging using Heterodyne Detection

Unlike traditional transport measurements, our imaging scheme is not limited to addressing only individually contacted devices, since each conducting pathway can produce photothermal current upon laser illumination. In fact, devices with more than one nanotube can be synthesized more easily with random growth and large electrode geometry, for which our heterodyne technique (Fig. 4a) can provide spatially resolved conductance information on single nanotubes as well.

The inset of Fig. 4b shows an optical image of a large-scale nanotube device **L1** with two interdigitated electrodes that lie on top of randomly grown nanotubes. Each quadrant is roughly 300 μm x 300 μm and the entire device consists of hundreds of nanotubes. On the right of Fig. 4b, we show a current image of the area outlined in red on L1 taken with heterodyne detection ($V_D > 0$). We note that because such multi-nanotube devices have a much higher noise floor, we can detect their current signals using only this high frequency detection scheme. The reflection image is again overlaid so that the electrodes are visible. We can clearly see the photothermal current from many nanotubes, with the strength of each signal reflecting the measure of conductance of each nanotube. An SPC image ($V_D = 0$) of the same scan area is shown on the left for comparison. While photocurrent is universally visible for most nanotubes, allowing us to

locate contacted nanotubes regardless of their conductance, photothermal current will be stronger for more conductive nanotubes. Indeed, most nanotubes can be seen in both images while several that have clear photocurrent spots (circled in white) do not show visible photothermal current and are most likely poorly conducting.
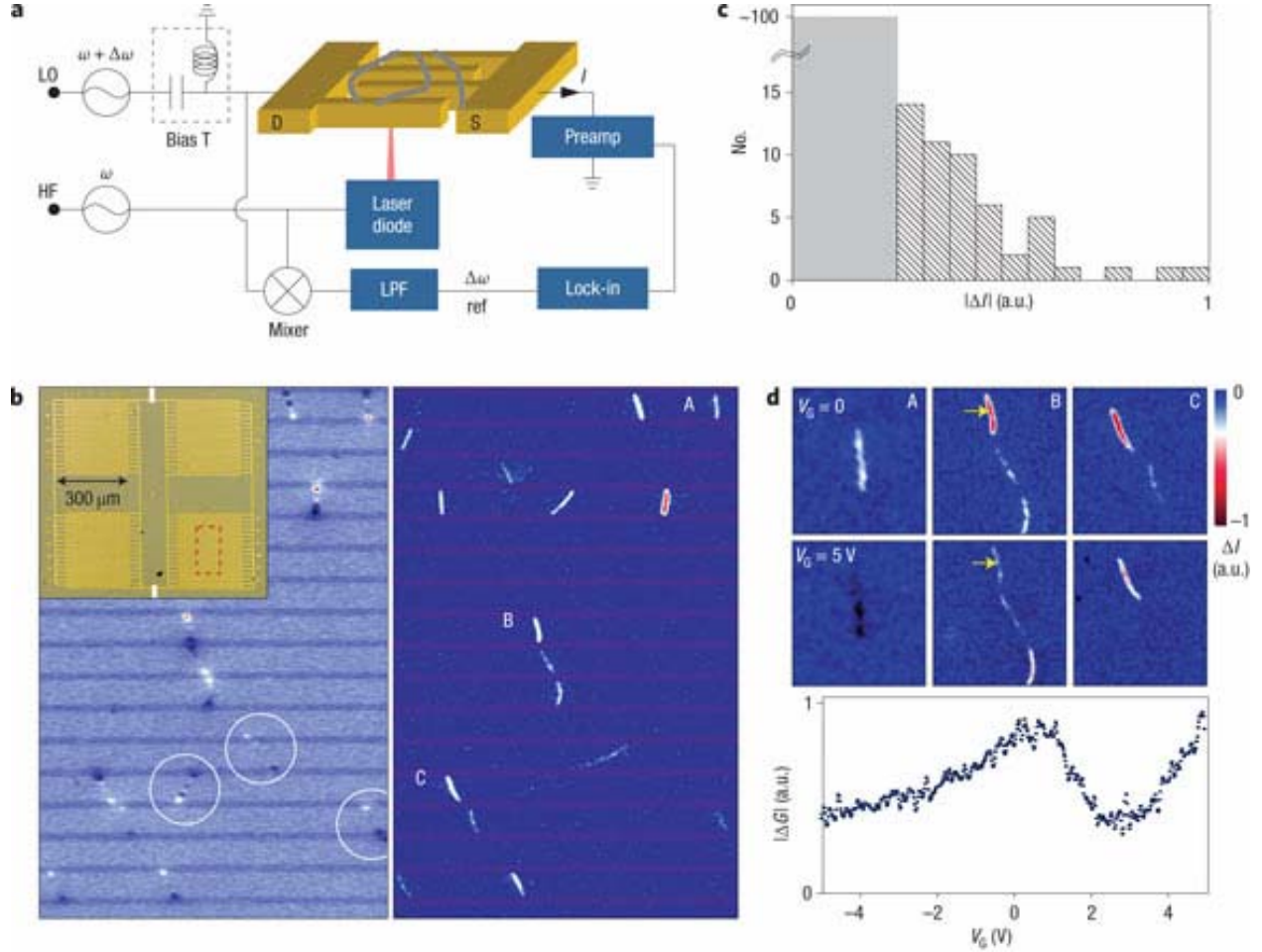
Fig. 4 a, Schematic of the heterodyne detection setup and the large-scale nanotube device under study. **b**, Inset: optical image of the large-scale carbon nanotube transistor L1 with interdigitated electrodes. Right: photothermal current image of the area outlined in red on L1 with $V_G = 0$. Left: photocurrent image ($V_D = 0$) of the same area. The circled spots are from poorly conducting nanotubes with no visible photothermal current. **c**, Distribution of photothermal current intensities for over 150 carbon nanotubes from large-area scans. The large bar denotes low-conductance nanotubes without photothermal current, but which are confirmed to exist through photocurrent scans. **d**, Top: photothermal images of nanotubes A, B and C from **b** at $V_G = 0$ and 5 V. Bottom: $|\Delta G|$ measured with the laser parked on the arrow on nanotube B versus V_G.

Using this scheme, we can qualitatively determine the relative conductance distribution for a large number of nanotubes. In Fig. 4c, we show a histogram of the photothermal current observed for over 150 nanotubes from large area scans. The large bar at the far left denotes low conductance nanotubes that are not resolved from photothermal imaging yet are confirmed to exist through SPC scans. From our previous analysis, we believe that this plot should scale closely with the nanotubes' absolute conductances, although a more detailed study will be required to develop a technique with better quantitative information.

It is also possible to determine the gate dependent conductance behaviour of individual nanotubes in this array geometry by studying how their photothermal current changes with V_G. In Fig. 4d (top), we show small area scans of nanotubes *A, B, C* from Fig. 4b at $V_G = 0$, 5 V, and we can see how each nanotube responds differently to the gate. In particular, nanotube *A* disappears at $V_G = 5$ V, indicating that it is a semiconducting nanotube. We also see that different segments of nanotubes B and C contacting different electrodes behave distinctly as well. To obtain more quantitative information, one can fix the laser on individual nanotube segments and measure the photothermal current (or ΔG) while continuously varying V_G (as shown in the bottom of Fig. 4d for the top segment of nanotube B).

D. Imaging Point Contacts in Pentacene Thin-Film Transistors

The performance of organic thin-film transistors (OTFTs) has improved significantly over the years[23,24]. However, achieving efficient charge injection in OTFTs is still a challenging issue, due to the presence of energy barriers at the electrode/organic film interface[25,26]. This particularly affects bottom-contact, bottom-gate OTFTs – i.e., the most relevant geometry for large-scale organic microelectronics.

We studied the spatially resolved, scanning laser-based study of the injection behavior of pentacene transistors with bottom-contact gold electrodes, a model-type OTFT [Fig. 5(a)]. In Fig. 5(b), we show typical output characteristics, from which we extract a hole field-effect mobility of ~ 0.2 cm^2/Vs at saturation, similar to that of other state-of-the-art pentacene OTFTs[23]. At low source-drain voltages, however, we observe a sigmoidal behavior, indicating the presence of an injection barrier. Correspondingly, our photoelectric measurements reveal that pentacene makes point-like electrical contacts to the gold, which could explain the limited hole-injection efficiency of such systems.

In the main panel of Fig. 6(a), we show a false color current image of a representative device for $V_{DS} = 0$, $V_{GS} = -20$ V with the grayscale reflection image overlaid for reference. While most of device is not electrically responsive to the laser, the current image exhibits striking spots of opposite polarity at the drain and source contacts. In Fig. 6(b), zoomed-in and separated reflection and current images of the green boxed area at the drain resolve the spots with greater clarity and reveal that they are located at the pentacene side of the interface, within the channel.

The effect of zero-bias "photocurrent" generation at metal/ semiconductor interfaces has been previously observed in nanostructure devices[30-33], and in the context of pentacene, can be explained by the electronic band diagram shown on top [Fig. 6(a)]. While the band structure of the pentacene bulk is made p-type by the gate, the levels are pinned at the contacts, resulting in a potential gradient at the interface. Here, photo-generated carriers separate and induce a current when collected, with sign dependent on the direction of band-bending[34].

All of the ~50 devices studied exhibit spot-like features of contact
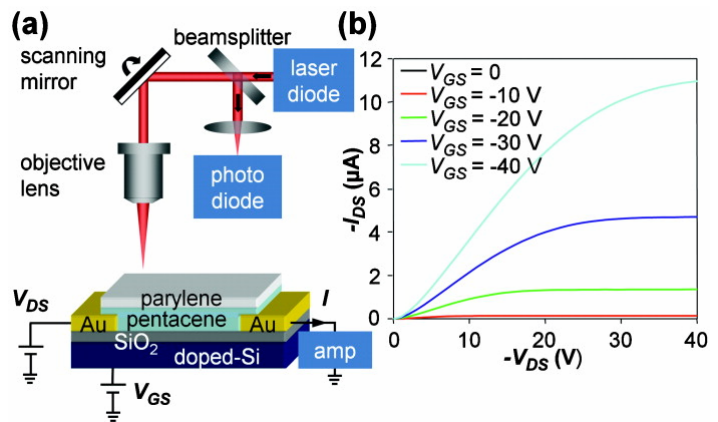
Fig 5 (a) Schematic of experimental setup. **(b)** Output characteristics of typical device.
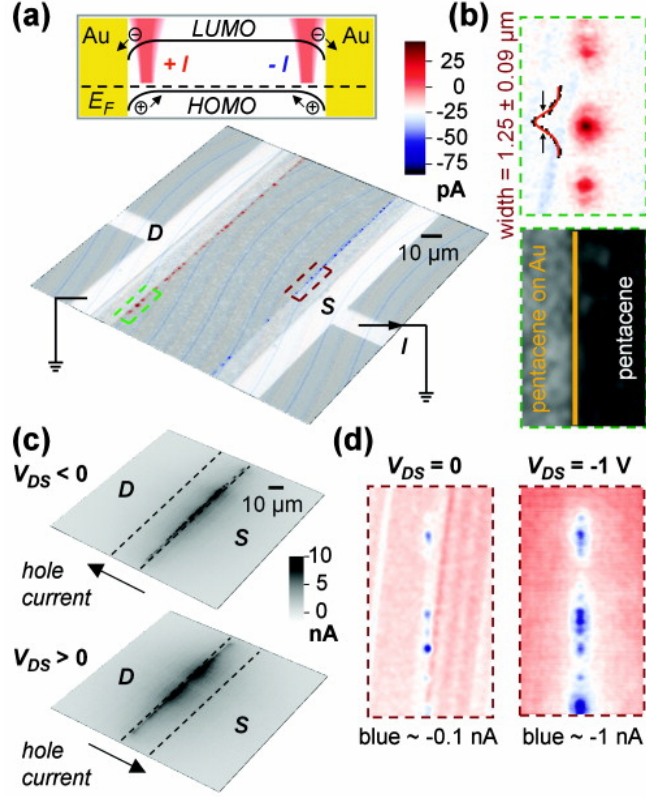
photocurrent. In addition, devices with greater number of spots demonstrate better electrical performance overall[35]. Substantiated by our measurements to follow, this strongly suggests that these spots correspond to good hole-injection contacts.

Furthermore, a line cut of the central spot in the zoomed-in current image is taken along the interface and fitted to a gaussian with width equal to the laser spot size. If pentacene formed extended electrical contact, we would expect an elongated signal. Instead, we observe point contacts to the gold within instrument limits. Therefore, despite the high pentacene film thickness ($\sim$ 50 nm), this gives compelling evidence that hole-injection occurs only at localized physical contacts to the first monolayers[36].

Fig 6 (a) Main panel: zero bias current image (false color) with reflection image overlaid (grayscale). Top: band diagram of pentacene. **(b)** Zoomed-in images of green boxed are in **(a)**. **(c)** Current images under applied source-drain bias. **(d)** Zoomed-in current images of red boxed area in **(a)** for zero and small bias. Colors are scaled differently for visual comparison.

E. Hole Injection and Resistance of an Individual Contact Point

When a drain bias is applied ($V_{DS} < 0$), a different effect is observed. At the top of Fig. 6(c), we show the current image $|I_{ph}|$ = $|I_{light} - I_{dark}|$ for another devcie with V_{DS} = -10 V. Now, the most striking response is present only at the source, or hole-injecting electrode, for which photo-generated current is two orders of magnitude larger than that at zero bias. A zoom-in of the red boxed area in Fig. 6(a) is shown in Fig. 6d for both V_{DS} = 0 and V_{DS} = -1 V. Their comparison reveals that the same contact points at the source seen from zero-bias photocurrent contribute to the larger signals under bias, suggesting that the laser assists in hole-injection (with electron-injection being negligible at the drain). The application of a positive bias for the device in Fig 6(c), V_{DS} = + 10 V, shows consistently, current features at the opposite (hole-injection) contact [Fig. 6(c), bottom].

Two distinct processes are responsible for this observed effect. The first is trap-induced photoconductivity[37,38], which is effective *throughout* our devices — photo-generated electrons can fall into shallow traps with long lifetime and attract additional holes from the source to increase current[39]. To verify this, in Fig. 7(a), we show the laser power dependence of $|I_{ph}|$ when the laser is fixed at three positions on a device for V_{DS} = -1 V, V_{GS} = 0: a contact spot at the source (arrow, left inset) and two areas within the channel (midgap and close to the drain electrode). All data show good fits to a power law with subunity exponent ($\sim$0.3 – 0.4), reflecting increased trap filling at higher light intensities[38].

More revealingly, we plot the ratios of $|I_{ph}|$ for the different positions as a function of laser power in the inset. $|I_{ph}|$ at the source especially dominates at lower powers and decreases relative to the photo-response at midgap at higher powers. In contrast, midgap / drain is nearly a constant, suggesting a different photoelectrical mechanism unique to the hole-injection contact.
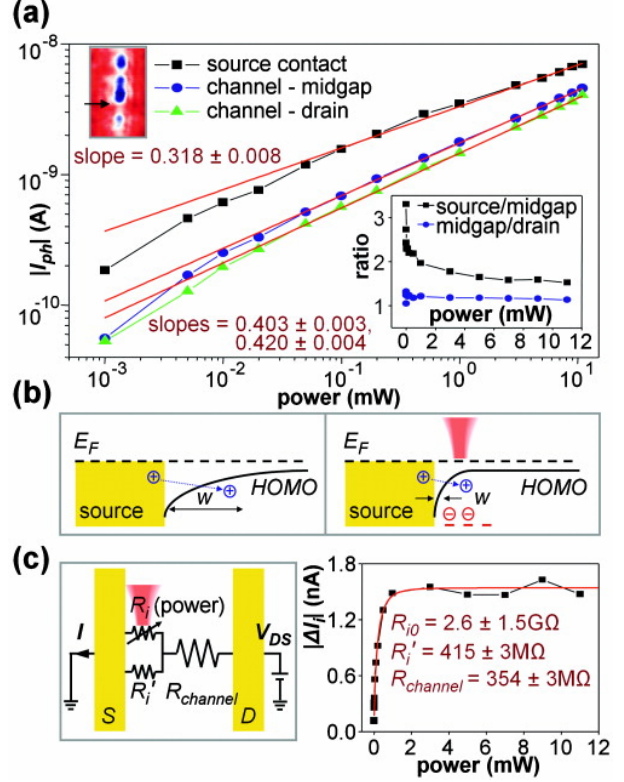
To explain this, we posit that localized, photo-induced electron traps at the source will alter the interfacial band structure. In general, holes injected from gold to pentacene must overcome a depletion barrier region (width w) where the bands are pinned [Fig. 7(b), left]. Previous scanning probe studies revealed that this translates to a large interfacial resistance R_i that can dominate overall device resistance[40,41]. Under illumination (right), the generated electron traps act as p-dopants of pentacene by attracting additional holes, reducing w and R_i. This is akin to semiconductor devices, where increased dopants around metal are used to lower contact resistance[42].

From these power dependence measurements, we can estimate R_i at an individual hole-injection point for $V_{GS} = 0$ using the following circuit model [Fig. 7(c), left]. The point contact illuminated above has a laser

Fig 7 (a) Main plot: power dependence of photogenerated current with laser at three positions on device. Inset: ratios of current vs power. **(b)** Band diagram of pentacene at source contact with and without illumination. **(c)** Left: circuit model for estimation of contact resistance. Right: current increase due to lowering of contact resistance vs laser power.

power- (or trap density-) dependent interfacial resistance $R_i(P)$, whereas non-illuminated contacts lump into R_i' in parallel and the bulk channel resistance $R_{channel}$ is in series. Under radiance of power P, we measure a current change corresponding to contributions from photoconductivity and reduction of interfacial resistance, $R_{i0} \rightarrow R_i(P)$:

$$I_{ph,source} = I_{light} - I_{dark} = \Delta I_{photocond.} + \Delta I_i = \Delta I_{photocond.} + \left(\frac{V_{DS}}{R_{channel} + R_i(P) \| R_i'} - \frac{V_{DS}}{R_{channel} + R_{i0} \| R_i'} \right). \quad (1)$$

ΔI_i can be extracted experimentally from the total change by subtracting the photo-response at midgap (where only photoconductivity is effective).

In Fig. 7(c) (right), we show $|\Delta I_i|$ as a function of P. At lower powers, $R_i(P)$ is large and close to the dark interfacial resistance R_{i0}, so $|\Delta I_i|$ is small. At higher powers, $R_i(P)$ vanishes and current saturates. A fit for the above expression yields $R_{i0} = 2.6 \pm 1.5$ GΩ for the point contact, $R_{channel} = 354 \pm 3$ MΩ, and $R_i' = 415 \pm 3$ MΩ [43]. We repeated this for another contact on the same device and obtained similar values.

F. Conclusion

In summary, we developed a nanotube conductance imaging technique ("photothermal current microscopy") based on the linear relationship between photothermal current induced by optical heating and the overall nanotube conductance. We expect the use of a tunable laser with this measurement scheme will allow for direct absorption spectroscopy of carbon nanotubes. Furthermore, the technique should be applicable to other linear nanostructures as well, including semiconducting nanowires[21], graphene nanoribbons[22], and nanofabricated conducting polymers. In addition, our spatially-resolved electrical studies of bottom-contact pentacene transistors reveal that pentacene makes point-like electrical contacts to the gold electrodes. When the device is under bias, they become hot spots that increase current dramatically when optically activated. Due to the diversity of organic/metal interfaces currently employed in OTFTs, we cannot claim our results to be universal. However, this work paves the way for a series of studies utilizing this photoelectrical technique to spatially identify and characterize the properties of OTFT contacts involving various organic semiconductor and contact materials.

G. References

1. Saito, R., Dresselhaus, G. & Dresselhaus, M. S. *Physical Properties of Carbon Nanotubes*. (Imperial College Press, 1998).
2. Jorio, A. *et al.* Carbon nanotube photophysics. *Mater. Res. Soc. Bull.* **29**, 276-280 (2004).
3. McEuen, P. L. & Park, J. Y. Electron transport in single-walled carbon nanotubes. *Mater. Res. Soc. Bull.* **29**, 272-275 (2004).
4. Avouris, P. Carbon nanotube electronics and optoelectronics. *Mater. Res. Soc. Bull.* **29**, 403-410 (2004).
5. Itkis, M. E., Borondics, F., Yu, A. P. & Haddon, R. C. Bolometric infrared photoresponse of suspended single-walled carbon nanotube films. *Science* **312**, 413-416 (2006).
6. Balasubramanian, K. *et al.* Photoelectronic transport imaging of individual semiconducting carbon nanotubes. *Appl. Phys. Lett.* **84**, 2400-2402 (2004).
7. Lee, E. J. H. *et al.* Electronic-band-structure mapping of nanotube transistors by scanning photocurrent microscopy. *Small* **3**, 2038-2042 (2007).
8. Freitag, M. *et al.* Imaging of the schottky barriers and charge depletion in carbon nanotube transistors. *Nano Lett.* **7**, 2037-2042 (2007).
9. Ahn, Y. H., Tsen, A. W., Kim, B., Park, Y. W. & Park, J. Photocurrent imaging of p-n junctions in ambipolar carbon nanotube transistors. *Nano Lett.* **7**, 3320-3323 (2007).
10. Purewal, M. S. *et al.* Scaling of resistance and electron mean free path of single-walled carbon nanotubes. *Phys. Rev. Lett.* **98**, 186808 (2007).
11. Zhou, X., Park, J.-Y., Huang, S., Liu, J. & McEuen, P. L. Band structure, phonon scattering, and the performance limit of single-walled carbon nanotube transistors. *Phys. Rev. Lett.* **95**, 146805 (2005).
12. Freitag, M., Martin, Y., Misewich, J. A., Martel, R. & Avouris, P. H. Photoconductivity of single carbon nanotubes. *Nano Lett.* **3**, 1067-1071 (2003).
13. Pankove, J. I. *Optical Processes in Semiconductors*. (Dover Publications, Inc., 1975).
14. Chen, R. J. *et al.* Molecular photodesorption from single-walled carbon nanotubes. *Appl. Phys. Lett.* **79**, 2258-2260 (2001).
15. Islam, M. F., Milkie, D. E., Kane, C. L., Yodh, A. G. & Kikkawa, J. M. Direct measurement of the polarized optical absorption cross section of single-wall carbon nanotubes. *Phys. Rev.Lett.* **93**, 037404 (2004).

16. Lauret, J. S. *et al.* Ultrafast carrier dynamics in single-wall carbon nanotubes. *Phys. Rev. Lett.* **90**, 057404 (2003).
17. Wang, F., Dukovic, G., Brus, L. E. & Heinz, T. F. Time-resolved fluorescence of carbon nanotubes and its implication for radiative lifetimes. *Phys. Rev. Lett.* **92**, 177401 (2004).
18. Maune, H., Chiu, H. Y. & Bockrath, M. Thermal resistance of the nanoscale constrictions between carbon nanotubes and solid substrates. *Appl. Phys. Lett.* **89**, 013109 (2006).
19. Lee, J. S. *et al.* Origin of gate hysteresis in carbon nanotube field-effect transistors. *J. Phys. Chem. C* **111**, 12504-12507 (2007).
20. Bockrath, M. *et al.* Resonant electron scattering by defects in single-walled carbon nanotubes. *Science* **291**, 283-285 (2001).
21. Lieber, C. M. Nanoscale science and technology: Building a big future from small things. *Mater. Res. Soc. Bull.* **28**, 486-491 (2003).
22. Obradovic, B. *et al.* Analysis of graphene nanoribbons as a channel material for field-effect transistors. *Appl. Phys. Lett.* **88**, 142102 (2006).
23. C. D. Dimitrakopoulos and P. R. L. Malenfant, Adv. Mater. **14**, 99 (2002).
24. R. A. Street, Adv. Mater. **21**, 2007 (2009).
25. J. C. Scott, J. Vac. Sci. Technol. A **21**, 521 (2003).
26. Y. L. Shen, A. R. Hosseini, M. H. Wong, and G. G. Malliaras, ChemPhysChem **5**, 16 (2004).
27. J. A. DeFranco, B. S. Schmidt, M. Lipson, and G. G. Malliaras, Org. Electron. **7**, 22 (2006).
28. A. W. Tsen, L. A. K. Donev, H. Kurt, L. H. Herman, and J. Park, Nat. Nanotechnol. **4**, 108 (2009).
29. M. Fiebig, C. Erlen, M. Gollner, P. Lugli, and B. Nickel, Appl. Phys. A: Mater. Sci. Process. **95**, 113 (2009).
30. Y. Ahn, J. Dunning, and J. Park, Nano Lett. **5**, 1367 (2005).
31. E. J. H. Lee, K. Balasubramanian, J. Dorfmuller, R. Vogelgesang, N. Fu, A. Mews, M. Burghard, and K. Kern, Small **3**, 2038 (2007).
32. M. Freitag, J. C. Tsang, A. Bol, D. N. Yuan, J. Liu, and P. Avouris, Nano Lett. **7**, 2037 (2007).
33. Y. H. Ahn, A. W. Tsen, B. Kim, Y. W. Park, and J. Park, Nano Lett. **7**, 3320 (2007).
34. http://dx.doi.org/10.1063/1.3462914
35. Y. Tsuruma, A. Al-Mahboob, S. Ikeda, J. Sadowski, G. Yoshikawa, Y. Fujikawa, T. Sakurai, and K. Saiki, Adv. Mater. **21**, 4996 (2009).
36. D. Knipp, D. K. Murti, B. Krusor, R. Apte, L. Jiang, J. P. Lu, B. S. Ong, and R. A. Street, *MRS Symposia Proceedings* No. 665 (Materials Research Society, Pittsburgh, 2001), p. C5.44.
37. J. Gao and F. A. Hegmann, Appl. Phys. Lett. **93**, 223306 (2008)
38. K. P. Puntambekar, P. V. Pesavento, and C. D. Frisbie, Appl. Phys. Lett. **83**, 5539 (2003).
39. A. Petrović, E. Pavlica, G. Bratina, A. Carpentiero, and M. Tormen, Synth. Met. **159**, 1210 (2009).
40. S. M. Sze and K. K. Ng, *Physics of Semiconductor Devices*, 3rd ed. (Wiley, New York, 2007).